ETH
Eidgenössische Technische Hochschule Zürich
Swiss Federal Institute of Technology Zurich

D PHYS

Maurice D. Hanisch
22-956-379

Towards a tunable beamsplitter interaction between two radial modes of two ions for GKP qubits

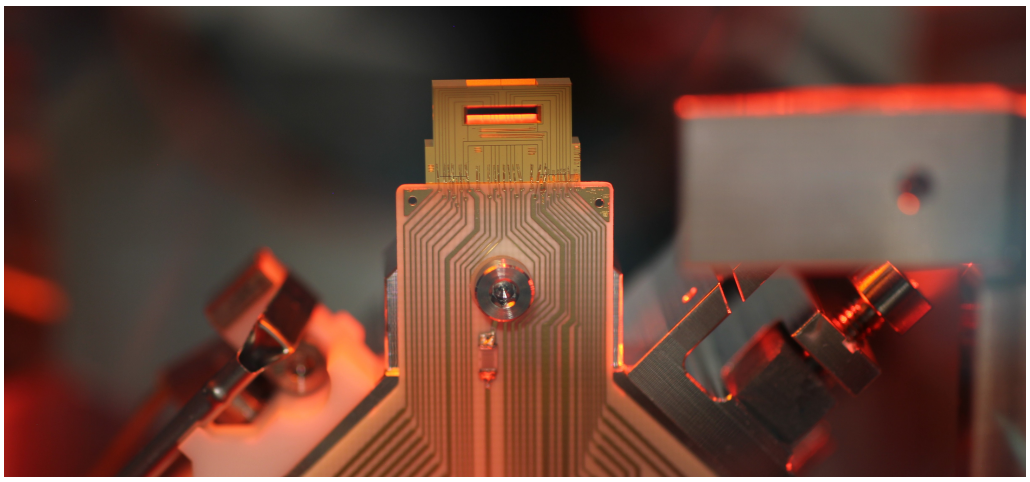

Semester Thesis

Master's Degree Programme in Physics
Trapped Ion Quantum Information Group (TIQI)
Swiss Federal Institute of Technology (ETH) Zurich

Supervision

Martin Wagener, Moritz Fontboté-Schmidt, Dr. Stephan Welte
Prof. Dr. Jonathan Home
July, 2023

Abstract

In this report, we investigate the implementation of a tunable beam splitter for a two-qubit gate between Gottesman-Kitaev-Preskill (GKP) encoded qubits. Emphasis is placed on achieving a decoupled setting at interion distances below 20 µm. Using numerical simulations with a model of the used trap, theoretical modal participation rates below 6% were found to be achievable. However, only experimental decoupling factors $\Delta\omega/2\Omega_B$ of at most 2.05 were achieved, corresponding to a theoretical 50% reduction in energy exchange between the two ions in the uncoupled setting. Consequently, we did not achieve sufficiently strong decoupling for the required switchable beamsplitter interaction. Future strategies could include working with lower quadratic potentials, exploring higher distance double wells, or manipulating interion distance in-sequence to control the coupling rate.

Acknowledgements

Firstly, I would like to thank Martin Wagener and Dr. Stephan Welte for teaching me the setup and supervising my project with constant support and great knowledge. I think I learned a lot about experimental work with you, and I thoroughly enjoyed it!

I also want to express my gratitude to Moritz Fontboté Schmidt. His open-mindedness towards fresh ideas, his willingness to explain in detail every process, and his infectious enthusiasm have made this project both very educational and, especially trying to get the last experimental data, extremely fun. I also want to thank him for his very valuable personal advices.

I would like to extend my sincere gratitude to Dr. Carmelo Mordini. His engaging discussions about the numerical aspects of the project contributed significantly to my understanding and have greatly enriched my perspective.

Lastly, I would like to express my appreciation to Prof. Jonathan Home for providing the opportunity to undertake this project in his group. Furthermore, his involvement and guidance during our weekly GKP group meetings have been significant in maintaining a clear vision of the project and directing its progression.

Contents

Chapter 1

Introduction

Quantum information processing proposes to solve computational problems that are to date intractable for classical computer, such as prime number factorization [19] or the elucidation of specific molecular reaction mechanism [16]. To achieve devices that can handle quantum information processing, the DiVincenzo's criteria [5] needs to be fulfilled. However, achieving long decoherence times, one of the criteria, has proven to be a significant issue. To remedy this task, quantum error correction (QEC) is necessary [14]. By encoding the quantum information in a redundant space, QEC protects the logical information against errors [12]. Given the overheads needed to do QEC with two-level systems, continous-variable systems have been considered as they provide inherent redundancy.

These, so-called "bosonic quantum encodings", can be implemented with trapped ions leveraging their motional states [9]. One such encoding, the Gottesman-Kitaev-Preskill (GKP) code [8], offers several advantages, notably is its potential for error correction as demonstrated by its "break-even" experiment [20, 1, 13]. Single qubit gates as well as error-correction for GKP states have been realized in trapped ions [7, 4]. However, to date, the implementation of two-qubit gates using GKP encodings remains a significant challenge.

One proposal of a realization of a two-qubit gate has been given by I. Rojkov [18], it can be decomposed into two single mode squeezing operations and one application of the beamsplitter. In a typical ion trap system, the beamsplitter interaction is naturally mediated through the Coulomb interaction. However, this also means that modes are constantly interacting, which is not desirable for a discrete two qubit gate. In this report, we address that issue and propose approaches to implement a tunable beamsplitter. Importantly, our approach focuses on developing a tunable beamsplitter that does not rely on moving the ions further apart to decouple them. This focus is due to the complexity of GKP encodings and the potential issues that could arise from the ions' movement.

Chapter 2 provides the theoretical groundwork necessary for understanding the beamsplitter implementation in our system. As the equilibrium positions of ions and the Coulomb interaction come into play, the problem becomes non-trivial to solve analytically, necessitating numerical methods. Hence, Chapter 3 delves into the numerical optimizations conducted to determine the optimal

voltage parameters for our experimental setup. The chapter outlines two approaches: a naive optimization over electrode voltages, and a more flexible approach using a lower-dimensional space to describe the resulting potential. We reached theoretical modal participation rates of 94% at interion distances below 20 µm. Finally, in Chapter 4, we present the results of our experimental efforts to reach an uncoupled system using our proposed methodologies. The chapter details our experimental setups and results for two ions trapped at an equilibrium position of approximately 12 micrometers, our attempts, and challenges in implementing a double well setup, and lastly a modified approach using a shallower quadratic to achieve higher ion distances. The highest decoupling factor $\Delta\omega/2\Omega_B$ we reached experimentally is 2.05 at 12 µm interion distance, thus, we did not achieve a strong enough decoupling for the needed switchable beamsplitter interaction.

Chapter 2

Theory

2.1 The calcium ion $^{40}Ca^{+}$

Quantum computation utilizing ions necessitates the most optimal control possible over the chosen qubit, consequently the use of the calcium ion ($^{40}Ca^{+}$) is widely spread as it possesses specific properties that are very useful for that task. The calcium ion is a monovalent cation of Calcium, an alkaline earth metal. Its electronic configuration in the ground state is [Ar]4s1, corresponding to a closed shell system with a single electron in the 4s orbital. This configuration, as seen in Figure 2.1, lends itself to a simple level diagram, facilitating ease of manipulation for quantum computing applications.

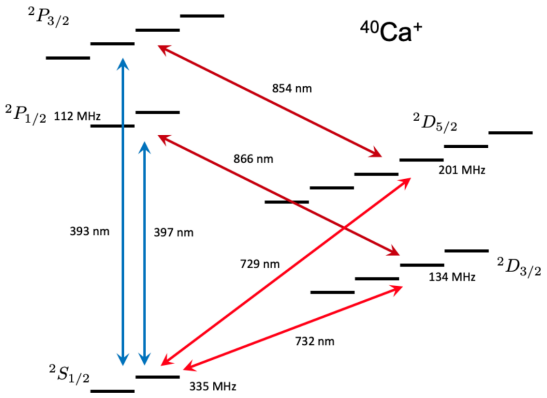

Figure 2.1: The energy level structure of $^{40}Ca^{+}$ is as follows. Typically, the $S_{1/2}$ state is chosen as the logical state $|0\rangle$, while the $D_{5/2}$ state is used as the logical state $|1\rangle$. The $S_{1/2} \leftrightarrow P_{1/2}$ transition has a wide linewidth and thus the $P_{1/2}$ state is employed for readout. The P3/2 and D3/2 levels need to be accounted for during the manipulation by possible repumping lasers. Taken from [9].

Two critical energy states in the electronic structure of $^{40}Ca^{+}$ are the $S_{1/2}$ (ground state) and $D_{5/2}$ (metastable excited state), known as the S-manifold and D-manifold, respectively. The qubit in a quantum computing system is typically encoded in these two states, with $|0\rangle$ state defined in the S-manifold and $|1\rangle$ state in the D-manifold.

The controlled transitions between these energy states in the $^{40}Ca^{+}$ ion are fundamental to the functioning of quantum operations. It is these transitions that form the basis for tasks such as state preparation, readout of the qubit state, and a universal set of gates.

One of the most notable transitions is the 397 nm dipole transition between the $S_{1/2}$ ground state and the $P_{1/2}$ excited state. This transition, driven by laser light, has a significant role in several vital operations in the quantum information processing domain.

- Doppler Cooling: This technique is used to reduce the motional energy of ions by employing momentum exchange between ions and laser photons. During this process, ions continuously absorb and emit laser photons, resulting in an overall reduction in their motional energy. The 397 nm dipole transition is ideally suited for Doppler cooling due to its relatively fast decay rate and thus fast cooling.

- Electromagnetically Induced Transparency (EIT) Cooling: EIT cooling is another technique to cool ions to temperatures below the Doppler limit. During EIT cooling, a quantum interference effect occurs, rendering the ions transparent to a particular wavelength of light. The 397 nm dipole transition is used in EIT cooling to couple the $S_{1/2}$ and $P_{1/2}$ states. See also [10].

- After computation, the 397 nm dipole transition plays a significant role in the measurement process. State-dependent fluorescence is used to determine the state of the ion, which is either in the "bright" state $|0\rangle$ if photons are scattered, or in the "dark" state $|1\rangle$ if after a certain time no photons are scattered.

Another important transition in the $^{40}Ca^{+}$ ion involves the $D_{5/2}$ state. This state is a metastable state with a relatively long lifetime of approximately 1s, making it suitable for storing quantum information. Transitions between the $S_{1/2}$ and $D_{5/2}$ states can be driven by laser light with a wavelength of approximately 729 nm, providing a basis for qubit manipulation and gate operations in quantum computation.

It's these well-controlled transitions that enable the use of $^{40}Ca^{+}$ ions for quantum information processing. They provide the basis for critical operations like state preparation, qubit manipulation, and state readout, further reinforcing the importance of understanding these transitions for advancing the field of quantum computing.

For more comprehensive insights into trapped-ion physics and the role of $^{40}Ca^{+}$ transitions, refer to the detailed lecture notes by D. Kienzler [9].

2.2 The GKP Setup trap

Results of this work have been achieved using a monolithic segmented 3D trap. It was fabricated using femtosecond lasers out of fused silica, coated with Ti/Au [15]. A model of the trap is depicted in Figure 2.2. The electrodes have sizes from 0.98 mm to 0.23 mm. Single addressing of the ions with the 729 nm laser is possible by two crossed AODs. Measuring the population of the $D_{5/2}$ state while scanning the frequencies of these AODs also allow to determine the positions of the ions [2, 21]. The reference publication is to come.

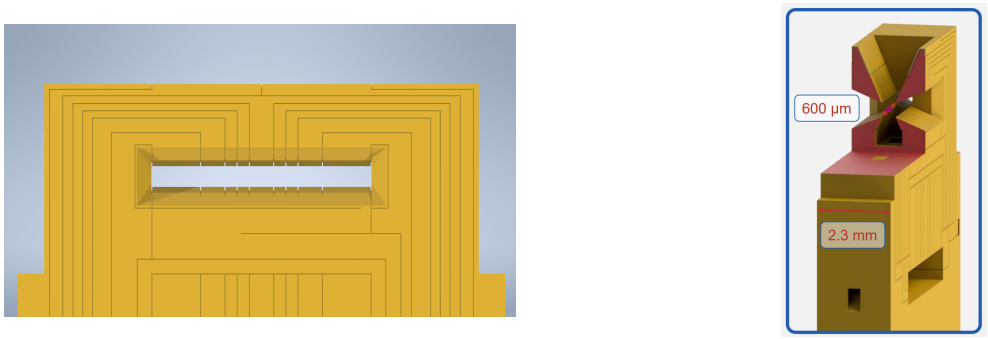

Figure 2.2: Illustration of the used monolithic segmented 3D trap. The electrodes have sizes of 0.98 mm, 0.48 mm, 0.23 mm and 0.625 mm for the central electrode.

2.3 Gottesman-Kitaev-Preskill encoding

An alternative to using internal electronic states to encode quantum information are bosonic encodings. Here, states of an harmonic oscillator are used. In trapped ions this is possible by using the harmonic motion of the ion in the trap.

An early proposal for such a bosonic encoding was the GKP code, named after Gottesman, Kitaev and Preskill [8]. The rise of interest for the GKP encoding is due to its ability to do fault-tolerant universal computation [8] and its potential for error correction, as shown by [1, 13]. Single qubit gates as well as error-correction for GKP states have been realized in trapped ions [7, 4]. Recently, "break-even" has been demonstrated in superconducting cavities, further highlighting the promise of GKP encodings [20].

These theoretical and experimental advantages come at the price of a relatively complex code space. Ideal GKP states consist of an infinite superposition of infinitely squeezed states. In particular, it can also be described with the stabilizer formalism, with operations given by commuting phase space displacements $\hat{\mathcal{D}}(\alpha)$. Such displacements follow specific commutation relations given by their geometric phase:

$$[\hat{\mathcal{D}}(\alpha), \hat{\mathcal{D}}(\beta)] = 2ie^{i\Phi}\sin(\Phi)\hat{\mathcal{D}}(\alpha)\hat{\mathcal{D}}(\beta), \text{ where: } \Phi = \mathrm{Im}\,(\beta\alpha^*) \tag{2.1}$$

Thus, displacements with $\Phi = k\pi, k \in \mathbb{Z}$ commute and displacements with $\Phi = (2k+1)\frac{\pi}{2}, k \in \mathbb{Z}$ anti-commute. Consequently, we can define our code space with following stabilizers and logical

operators:

$$\begin{aligned}
&\hat{\mathcal{D}}(l/2) = \hat{X}_L \approx \hat{X}_L^\dagger = \hat{\mathcal{D}}(l/2)^\dagger = \hat{\mathcal{D}}(-l/2) \\
&\hat{\mathcal{D}}(i\pi/l) = \hat{Z}_L \approx \hat{Z}_L^\dagger = \hat{\mathcal{D}}(i\pi/l)^\dagger = \hat{\mathcal{D}}(-i\pi/l) \\
&\hat{\mathcal{D}}(-l/2 - i\pi/l) = \hat{Y}_L \approx \hat{Y}_L^\dagger = \hat{\mathcal{D}}(l/2 + i\pi/l) \\
&\hat{S}_X = \hat{\mathcal{D}}(l) \approx \mathbb{1}_L \\
&\hat{S}_Z = \hat{\mathcal{D}}(2i\pi/l) \approx \mathbb{1}_L.
\end{aligned} \tag{2.2}$$

We can visualize the operations in a grid-like structure as shown in Figure 2.3.

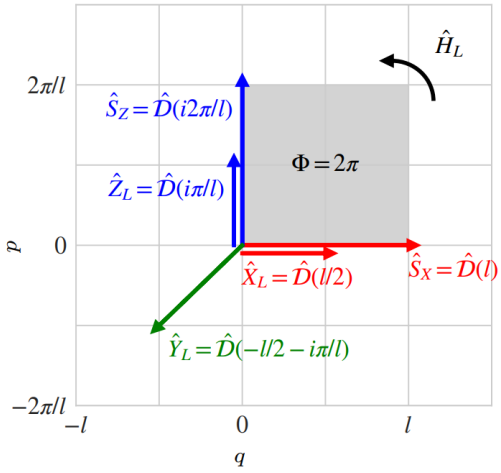

Figure 2.3: Phase space displacements for the two stabilizer operators $\hat{S}_X$, $\hat{S}_Z$ and the logical Pauli operators $\hat{X}_L, \hat{Y}_L, \hat{Z}_L$ shown is also the relevant phase space area Φ. The Hadamard operation is given by a $\pi/2$ rotation of phase space together with a rescaling of the phase space axis. Taken from [6]

Consequently, the code space, given by the intersection of the $+1$ eigenspace of the stabilizers, has ideal logical states:

$$\begin{aligned}
|0\rangle_{L,\mathrm{id}} &= \sum_{k=-\infty}^{\infty} \hat{\mathcal{D}}(kl)|q=0\rangle \\
|1\rangle_{L,\mathrm{id}} &= \hat{X}_L|0\rangle_{L,\mathrm{id}} = \sum_{k=-\infty}^{\infty} \hat{\mathcal{D}}(kl + l/2)|q=0\rangle
\end{aligned} \tag{2.3}$$

where $|q=0\rangle$ is the position 0 eigenstate.

As can be directly seen by their form, the ideal code words are unphysical because they represent states of infinite energy and cannot be normalized. However, one can approximate such states using finite superpositions of displaced finitely squeezed states [8]:

$$|0\rangle_L = \sum_{k\in\mathbb{Z}}^{\pm|k_{\max}|} c_k \hat{\mathcal{D}}(kl)\hat{\mathcal{S}}(r)|q=0\rangle \qquad |1\rangle_L = \hat{X}_L|0\rangle_L \tag{2.4}$$

with $\hat{\mathcal{S}}(r)$ the position squeezing operator and c_k real weights following some distribution, where the ideal states are reached in the limit of $r, k_{max} \to \infty$. Using such approximate states will lead to logical errors, however those errors are quantifiable and thus can be accounted for in the

overall error budget [8]. The Wigner functions of such approximate states for two different sets of parameters can be seen in Figure 2.4.

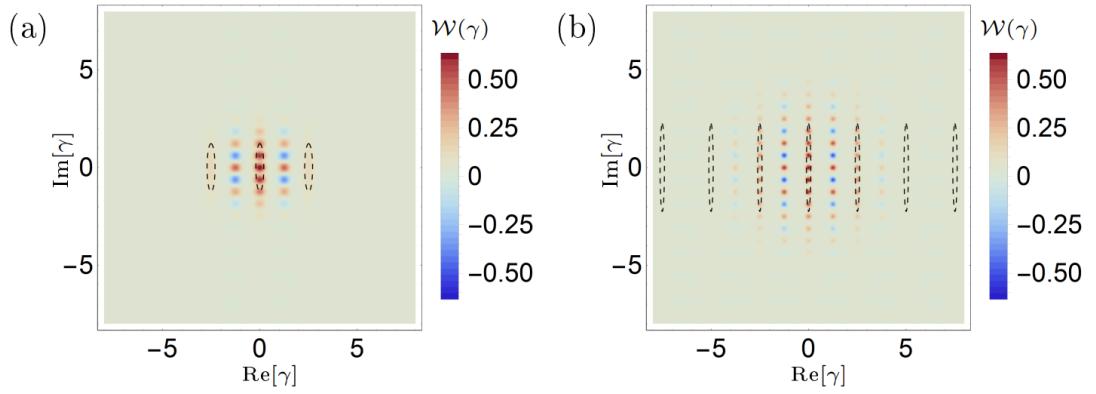

Figure 2.4: Two examples of approximate $|0\rangle_L$ states. (a) r = 0.9, $k_{max} = 1, c_0/2 = c_1 = c_1$. (b) r = 1.5, $k_{max} = 3, c_0 = 4c_{\pm 1}/3 = 10c_{\pm 2}/3 = 20c_{\pm 3}$. The dashed ellipses help as a guide to the eye and show the r.m.s extent of the squeezed components used to built up the states. The interference between these components leads to the build up of the 2D grid in phase space. For more components and higher amounts of squeezing (b) the grid becomes larger while simultaneously the individual features become narrower. The limit of ideal code states is given by an infinite grid of delta peaks. Taken from [6]

2.4 Two qubit gates for finite energy GKP states

As previously discussed, the increase in interest for GKP encodings is due to its universal gate-set that can be implemented fault-tolerantly[1], such universal gate-set typically consists of a set of universal single-qubit rotations and one complementary two-qubit gate such as a CNOT or a CZ. The former has been shown to be implementable [7], however, to date, the implementation of a two-qubit gate on GKP-encoded qubits has not been shown.

There are multiple possible approaches to tackle this task, one of them is presented in the theoretical considerations of I. Rojkov et al. [18], where a technique was proposed that specifically considered finite energy GKP states which are obtained by applying an "envelope operator" $\hat{E}_\Delta = e^{-\Delta^2 \hat{n}}$ on the initial ideal state according to $|\psi\rangle_\triangle \propto \hat{E}_\Delta |\psi\rangle_{\text{id}}$, where $\hat{n} = \frac{1}{2}\left(\hat{q}^2 + \hat{p}^2\right)$ is the number operator and Δ parameterizes the size of the envelope in phase space. There it was shown that a CZ gate, which is the missing element to get a full universal gate-set starting from what has already been implemented experimentally in the past, can be decomposed into two squeezing operations and one application of the beamsplitter:

$$\text{CZ}(\theta, r) = \hat{S}^{\otimes 2}(r)\hat{B}_A(\theta)\hat{S}^{\otimes 2}(-r) \tag{2.5}$$

with $\hat{S}^{\otimes 2}(r) = \hat{S}(r) \otimes \hat{S}(r)$ and $\hat{S}(r) = e^{i\frac{1}{2}r(\hat{q}_j\hat{p}_j + \hat{p}_j\hat{q}_j)}$ the squeezing operation on mode j, and with $\hat{B}_A(\theta) = e^{i\theta(\hat{q}_1\hat{q}_2 + \hat{p}_1\hat{p}_2)}$ the anti-symmetric beamsplitter transformation [18].

[1] Under certain assumptions on the ancilla.

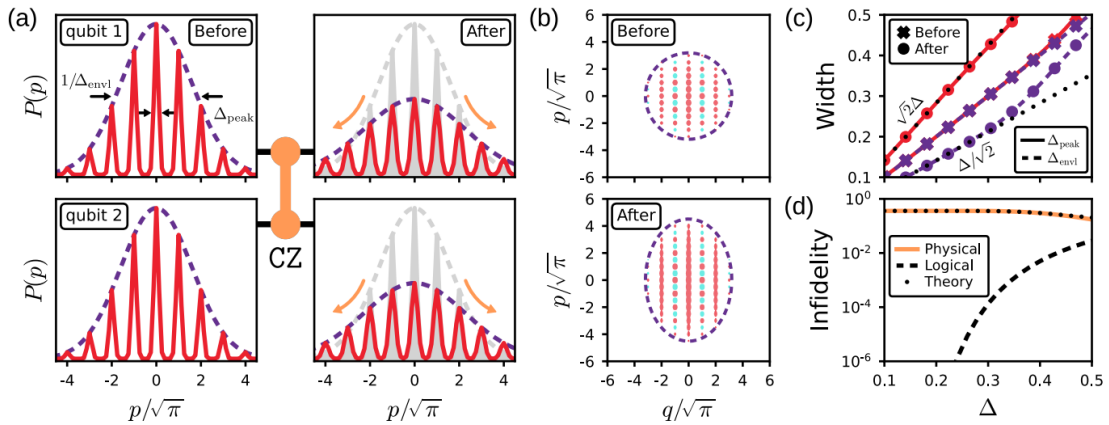

Figure 2.5: Finite-energy effects in two GKP qubit operations can be described as follows: (a) The momentum marginal distribution $P(p)$ for both oscillators, which are initially in the state $|0\rangle_\Delta$, undergoes a transformation due to the CZ gate. Before the operation, the state exhibits a specific distribution (depicted on the left) which is altered post-operation (shown on the right). The output distributions experience broadening because the operation corresponds to a continuous set of displacements. This broadening disperses each oscillator's wave function, conditioned on the position of the other oscillator. (b) The Wigner quasiprobability distribution illustrates broadening solely in the p quadrature. (c) The width of the peaks as a function of the input width clearly portrays a linear relationship. (d) The physical and logical infidelity between the input and output states as a function of the energy parameter, denoted by Δ, is also presented. The infidelity measures the discrepancy between the initial and final states, which is directly influenced by the energy parameter. Taken from [18]

However, this gate is intended to work on ideal GKP states, consequently, if applied on finite energy GKP states, so called "finite-energy effects" would occur, as shown in Figure 2.5.
Two circumvent these effects, two methods were proposed:

- Locally correct for small shifts in the phase-space and for deformations of the energy envelope using **quantum error correction procedures** before and after the CZ gate.
- Use a **modified version of the CZ gate**, called finite-energy version, which is obtained by conjugating the gate with the envelope operator $\hat{U}_\Delta = \hat{E}_\Delta \hat{U}_\text{I} \hat{E}_\Delta^{-1}$.

Consequently, we now have at our disposition a method to implement a two-qubit gate while accounting for the experimental limitation of only having access to some finite energy states. Furthermore, this method only needs squeezing operations and a beamsplitter operation. The theory and implementation of the later will be the main focus of this paper.

2.5 Coupled harmonic oscillators and the beamsplitter interaction

2.5.1 Coulomb interaction

For trapped ions, the coulomb interaction between the ions can be utilized to implement the beamsplitter interaction. In fact, considering only two ions for now, if we approximate the coulomb

potential for small displacements relative to the equilibrium position distance, we get:

$$\begin{aligned} U\left(\hat{\mathbf{r}}_1, \hat{\mathbf{r}}_2\right) &= \frac{q_1 q_2}{4\pi\epsilon_0} \frac{1}{|\hat{\mathbf{r}}_1 - \hat{\mathbf{r}}_2|} = \frac{q_1 q_2}{4\pi\epsilon_0} \frac{1}{|\hat{\mathbf{x}}_1 - \hat{\mathbf{x}}_2 - \mathbf{s}_0|} \\ &\approx \frac{q_1 q_2}{4\pi\epsilon_0} \left(\frac{1}{s_0} + \cos(\gamma) \frac{\hat{x}_1 - \hat{x}_2}{s_0^2} + \left(1 - 3\cos^2(\gamma)\right) \frac{-\hat{x}_1^2 - \hat{x}_2^2 + 2\hat{x}_1\hat{x}_2}{2s_0^3} \right), \end{aligned} \tag{2.6}$$

with $\hat{\mathbf{r}}_1$ and $\hat{\mathbf{r}}_2$ the position vectors of the two ions, $\hat{\mathbf{x}}_1$ and $\hat{\mathbf{x}}_2$ the displacements from their equilibrium positions, $\mathbf{s}_0$ is the distance vector between both equilibrium positions and $|\mathbf{s}_0| = s_0, |\hat{\mathbf{x}}_{1,2}| = \hat{x}_{1,2}$. Furthermore, γ is the angle between $\hat{\mathbf{x}}_1$ (here we are assuming that both ions are displaced in parallel directions) and $\mathbf{s}_0$.

Each term can be interpreted in the following way:

- The first term $\frac{1}{s_0}$ is constant and just adds a potential offset which does not affect the system.
- The second term $\cos(\gamma)\frac{\hat{x}_1 - \hat{x}_2}{s_0^2}$ is linear in the position, and so produces a constant force that displaces both ions in opposite directions.
- The third term $\left(1 - 3\cos^2(\gamma)\right)\frac{-\hat{x}_1^2 - \hat{x}_2^2}{2s_0^3}$ induces a constant change in the trap frequency of both ions, this effect can also be counteracted by a quadratic term in the applied voltages.
- From the last term $\left(1 - 3\cos^2(\gamma)\right)\frac{\hat{x}_1\hat{x}_2}{s_0^3}$ we get the coupling needed for our beamsplitter:

Expressing the positions operators in terms of ladder operators we get:

$$\hat{H}_B = \left(1 - 3\cos^2(\gamma)\right) \frac{q_1 q_2}{4\pi\epsilon_0} \frac{\hat{x}_1\hat{x}_2}{s_0^3} \tag{2.7}$$

$$= -\hbar\Omega_B(\gamma) \left(\hat{a}_1 + \hat{a}_1^\dagger\right) \left(\hat{a}_2 + \hat{a}_2^\dagger\right) \tag{2.8}$$

$$\overset{\text{RWA}}{=} -\hbar\Omega_B(\gamma) \left(\hat{a}_1\hat{a}_2^\dagger + \hat{a}_1^\dagger\hat{a}_2\right), \tag{2.9}$$

where in the last step we used the rotating wave approximation and discarded fast rotating terms. Thus, we get a term that corresponds to our needed beamsplitter interaction with a coupling rate of:

$$\Omega_B(\gamma) = \left(1 - 3\cos^2(\gamma)\right) \frac{q_1 q_2}{8\pi\epsilon_0 s_0^3 \sqrt{m_1 m_2}\sqrt{\omega_1\omega_2}}. \tag{2.10}$$

Such beamsplitter interactions have been implemented in trapped ions, where different effects including the Hong-Ou-Mandel effect and coherent energy exchange have been shown [3, 24].

2.5.2 Classical coupled harmonic oscillators

In fact, this interaction may be understood as two coupled harmonic oscillators. The coupling Hamiltonian is given by

$$\hat{H}_B = \left(1 - 3\cos^2(\gamma)\right) \frac{q_1 q_2}{4\pi\epsilon_0} \frac{\hat{x}_1\hat{x}_2}{s_0^3}, \tag{2.11}$$

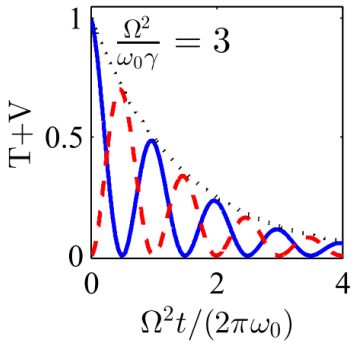

Figure 2.6: Resonant: With $\omega_1 = \omega_2 = \omega_0$ the bare frequencies of the oscillators and $\gamma_1 = \gamma_2 = \gamma$

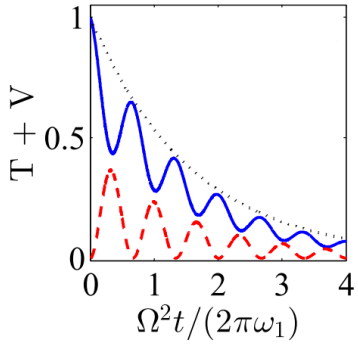

Figure 2.7: Detuned: $\omega_1 = 1\text{rads}^{-1}$, $\omega_2 = 0.989\text{rads}^{-1}$, $\Omega_1 = 0.1\text{radm}^{-1}$ and $\gamma_1 = \gamma_2 = \gamma = 1\text{mrads}^{-1}$.

Figure 2.8: Time evolution of the total energy in two coupled harmonic oscillators. The blue solid line is the energy in oscillator 1, the red dashed line is the energy in oscillator 2, and the dotted black line is $e^{-2\gamma t}$. Taken from [17]

thus giving us coupled equations of motions of the form:

$$\begin{aligned} \ddot{x}_1 + \gamma_1\dot{x}_1 + \omega_1^2 x_1 - \Omega_B^2 x_2 = 0, \\ \ddot{x}_2 + \gamma_2\dot{x}_2 + \omega_2^2 x_2 - \Omega_B^2 x_1 = 0. \end{aligned} \tag{2.12}$$

with some constants $\gamma_{1,2}$ representing the damping rates, which in our model are 0, and the coupling rate $\Omega_B = 2 \cdot \Omega_B(\gamma) \cdot \sqrt{m_1 m_2}\sqrt{\omega_1\omega_2}$ between both oscillators. Such a system can be solved analytically and if we take a look at the energy of the individual oscillators we see a coherent exchange of energy over time. Furthermore, the contrast and the frequency of this energy exchange is determined by the detuning of the two oscillators, as seen in Figure 2.8. Thus, if the bare frequency of the two oscillators are detuned, the energy is not fully exchanged and also the frequency of the oscillation is increasing.

2.5.3 Coupled quantum harmonic oscillators

Furthermore, we can generalize that result to the quantum case. Solving the Heisenberg equations for the evolution of the raising and lowering operators under Eq. 2.9 we get:

$$\begin{pmatrix} \dot{a}_1^\dagger \\ \dot{a}_2^\dagger \end{pmatrix} = i \begin{bmatrix} \omega_1 & \Omega_B \\ \Omega_B & \omega_2 \end{bmatrix} \begin{pmatrix} a_1^\dagger \\ a_2^\dagger \end{pmatrix} \tag{2.13}$$

which results in:

$$\begin{aligned} a_1^\dagger(t) &= e^{i\bar{\omega}t}\left[a_1^\dagger(0)\left(\cos\tilde{\Omega}t + \frac{\Delta\omega}{2\tilde{\Omega}}\sin\tilde{\Omega}t\right) + ia_2^\dagger(0)\frac{\Omega_B}{\tilde{\Omega}}\sin\tilde{\Omega}t\right] \\ a_2^\dagger(t) &= e^{i\bar{\omega}t}\left[a_2^\dagger(0)\left(\cos\tilde{\Omega}t - \frac{\Delta\omega}{2\tilde{\Omega}}\sin\tilde{\Omega}t\right) + ia_1^\dagger(0)\frac{\Omega_B}{\tilde{\Omega}}\sin\tilde{\Omega}t\right], \end{aligned} \tag{2.14}$$

with $\bar{\omega} = (\omega_1 + \omega_2)/2$, $\Delta\omega = |\omega_1 - \omega_2|/2$ and $\tilde{\Omega} = \frac{1}{2}\sqrt{4\Omega_B^2 + \Delta\omega^2}$.

Similar to the classical case, we see that the raising operator for mode a transforms in a sum containing terms with the raising operator of mode b, hence we can also see this energy exchange for the quantum case. More specifically:

- for $\Delta\omega = 0$, thus $\tilde{\Omega} = \Omega_B$, we have $a_1(t = \frac{\pi}{2\Omega_B}) = ia_2(0)$, hence there is a full energy oscillation from the first to the second quantum oscillator.
- for $\Delta\omega \neq 0$, our oscillations do not reach full contrast, and we also have $\tilde{\Omega} > \Omega_B$ thus the energy transfer is happening on faster timescales. In fact, one can just connect these results to resonant/detuned Rabi oscillations.

These classical and quantum mechanical considerations give the needed tools to implement a theoretical switchable beamsplitter:

- To get an **uncoupled setting**, where we do not want the two oscillators to exchange energy, we need to have the detuning much bigger than the coupling rate: $\Delta\omega >> \Omega_B$, thus resulting in very low contrast energy exchange oscillations.
- To get a **coupled setting**, where we do want two oscillators to fully and quickly exchange energy, we need to have the coupling rate to be much bigger than the detuning $\Delta\omega << \Omega_B$, resulting in full contrast oscillations with frequency Ω_B.

2.5.4 How to experimentally verify the coupling

We now know what parameters need to be changed to achieve the tunable beamsplitter, however we still need to be able to measure what coupling we managed to reach in the experiment. To do so, we have two possibilities:

-Avoided crossing diagram: The eigenmodes of our system can be found by diagonalizing Eq. 2.9, resulting in "in-phase" and "out-of-phase" modes with energies

$$\omega_{in/out} = \bar{\omega} \pm \tilde{\Omega} = \bar{\omega} \pm \frac{1}{2}\sqrt{4\Omega_B^2 + \Delta\omega^2}. \tag{2.15}$$

These modes will be the one we will see in our experiment if the timescale of our measurement are long compared to the inverse of the coupling rate between our ions. For a fixed coupling rate, the frequencies of the two eigenmodes of the system can be plotted as a function of the detuning of the local modes. The resulting plot is a so called "Avoided Crossing" as can be seen in Figure 2.9. This graph can be experimentally generated by measuring the eigenmode frequencies via a detuned carrier absorption spectrum, while maintaining a constant coupling rate. This can be achieved by holding the equilibrium distance s_0 constant and altering the detuning of the two ion frequencies via voltage adjustments. The minimal detuning between the two frequencies, which gives twice the coupling rate, can then be observed. Moreover, by comparing this minimal detuning to the maximal detuning between frequencies, we can quantify the decoupling. However, this method is quite tedious, because, as we will see in the next chapter, to keep the distance constant the voltage parameters have to be readjusted. Being able to infer the coupling parameters from just

one certain voltage setting would be much more beneficial. To do so, one could measure the two ion distance to compute the coupling rate, then measure the detuning of the two eigenmode frequencies and calculate the detuning divided by 2 coupling rates, which also corresponds to the ratio of the waist of the anti-crossing graph to the maximal detuning. This quantity would then indicate how decoupled the two ions are. Furthermore, one can calculate the ratio of the energy exchange, plugging

$$\frac{|\Delta\omega_{in/out}|}{2\Omega_B} = \frac{\tilde{\Omega}}{\Omega_B} \tag{2.16}$$

in $ia_k^\dagger(0)\frac{\Omega_B}{\tilde{\Omega}}\sin\tilde{\Omega}t$ of Eq. 2.14 giving the inverse prefactor of the energy oscillation.

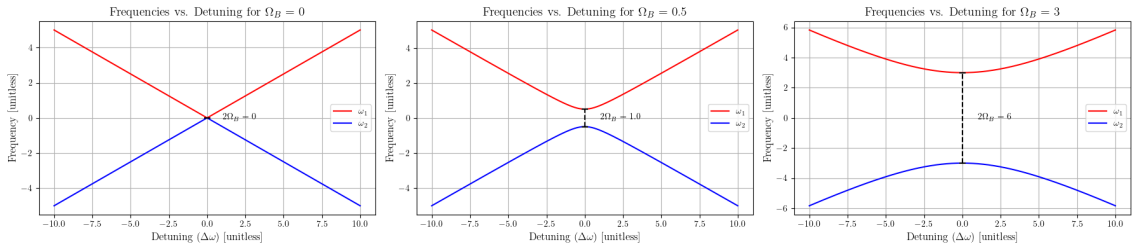

Figure 2.9: Avoided crossing diagram for unitless variables.

-Participation rates: Another possibility to assert how uncoupled our ion system is for one voltage setting is to measure the "participation rates" of our ions. In a perfectly uncoupled setting, each single mode will represent the movement of only a single ion, however in a perfectly coupled system the motional solutions are the in-phase and out-of-phase modes, where both ions move with equal amplitudes. Consequently, to measure how uncoupled the ions are, one could envision to measure the relative coupling strength of the side bands to the carrier for each ion, thus retrieving the motional participation rates of each ion for a certain mode. This metric will likewise allow quantifying the reached decoupling in the experiment.

To sum up, we have now grasped the method for implementing a beamsplitter interaction, and we have devised theoretical approaches for establishing both coupled and uncoupled system configurations. Furthermore, we have identified two verification methods for affirming the correspondence of our theoretical constructs within the experimental setup. Nevertheless, we will mainly use the avoided crossing approach due to its simplicity and sufficiency for our purposes at the moment. The remaining task is to determine the optimal theoretical setup parameters, specifically, the most suitable voltage settings that will facilitate the realization of these uncoupled/coupled configurations. Trivially, the coupled configuration is just a symmetric setting where both ions are minimally separated and feel the same potential, thus we will only consider how to achieve the uncoupled state in the next chapters.

Chapter 3

Numerical Optimizations

After understanding the theoretical framework for implementing the beamsplitter, our next task is to identify the optimal voltage parameters to put the theory into practice. However, the issue becomes challenging to solve analytically due to the necessity of considering the equilibrium positions of our ions while factoring in the Coulomb interaction. Therefore, to obtain the required theoretical parameters for the uncoupled and coupled settings, we proceed using numerical methods. This way one can also directly account for the trap model, as the simulations for the potential of each electrode has already been done and can be used.

In the following, we will present numerical methods and approaches that can be used to orient experimental efforts. The main idea of this chapter lies in using numerical optimizations over different sets of parameters to optimally decouple the radial modes. The parameters that can be changed in the setup are the 9 pairs of electrode voltages[1] and in the following we propose two approaches. On one hand, we naively optimize over those 9 parameters, however this approach does not give us enough flexibility to interpret and thus manually correct for experimental variation in the setup. Consequently, we also embed the problem in a lower dimensional space by describing the resulting potential with a polynomial of up to fourth order. This affords leverage on the physical interpretation of each parameter and allows for small corrections during the experiment. Finally, we will also discuss the limitations of the numerically found results.

3.1 Optimization over electrode voltages

Ultimately, we seek to encode the GKP state in the radial modes because the frequency in those modes is higher than the axial frequency, which should give, among others, advantageous lower heating rates. Thus, the idea we will follow in this work is to find a set of electrode voltages that result in a certain equilibrium distance and where the radial modes are as detuned as possible to reach the uncoupled beamsplitter setting. In fact, controlling the radial frequency with an axial potential is quite straightforward, as applying a constant DC voltage on the axial electrodes will "squeeze" the radial potentials and change the resulting radial frequencies approximately linearly.

[1] In fact, as described in Chapter 2 we have 22 electrodes, however, we will disregard the 4 shim electrodes as they are only used for micromotion compensation, and we will also set the bottom and top electrodes on the same voltages to stay in the RF null.

This linear dependence can be seen in Figure 3.1, where we used our trap model, added an initial 0.3MHz quadratic potential at the trap center to a constant offset of variable voltage and plotted the radial frequencies of all 3 modes for 2 ions. We can see that the evolution of both radial mode frequencies can be approximated as linear, where one is increasing and one is decreasing. The effects at the lower and higher ends of offset voltages are likely numerical errors.

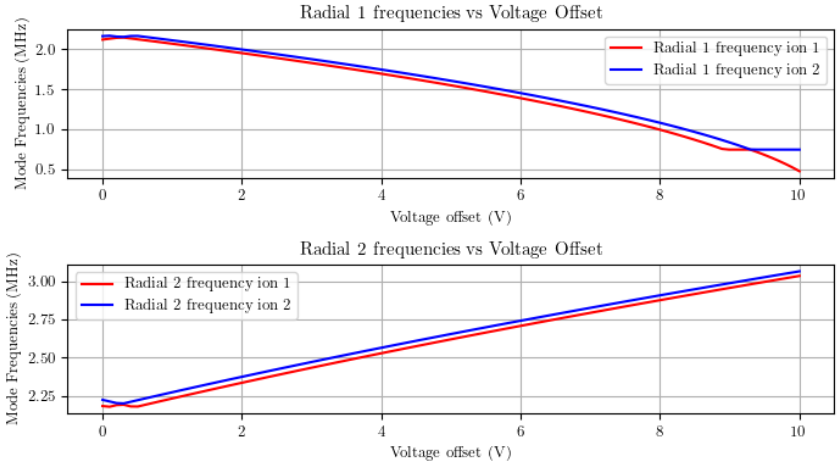

Figure 3.1: Mode frequencies for two calcium ions in a 0.3MHz quadratic potential and an added constant offset voltage.

As a consequence, to achieve a detuned setting in theory one could just have a quadratic potential, and then add a step function in the voltages such that the voltage at the axial positions of ion 1 is different from the voltage at the axial position of ion 2. This would ensure that the radial frequencies of the two ions are very detuned and thus for a fixed distance one could arbitrarily decouple them. However, it is important to note that from Eq. 2.6 we can see that we could also strongly influence the coupling by changing the equilibrium distance s_0. Nevertheless, this would mean that to have a switchable beamsplitter one would need to move the two ions around, and this would imply many complications, especially when working with very complex motional states like GKP states. Consequently, we chose the approach to decouple the ions at the smallest possible distance by trying to get the decoupling from the detuning of their frequencies via an offset. However, in practice, adding such a step function is limited by the maximum allowable voltages and also the finite electrode sizes. Without giving intensive thought to which approach is best to obtain two equilibrium positions that have very different offsets, we begin our numerical approach quite naively by defining a cost function that describes our coupling, and then minimize this function numerically over the parameter space of the 9 voltages.

3.1.1 The cost function

We want the cost function to be a good metric for our coupling, thus, as described in Chapter 2 we consider two options.

On one hand, the primary condition for an uncoupled setting can be expressed as $\Delta\omega << \Omega_B$. By assuming that the ions are displaced in parallel directions, similar to the approximation used in equation 2.6, we can diagonalize each of the 3x3 submatrices of the total Hessian[2] simultaneously. Consequently, the 3D coupled system reduces to 3 independent instances of 1D coupled systems, where each of this instance corresponds to 1 spatial direction. For our case, those directions are the axial and the 2 radial directions. Thus, for each direction we get an independent equation of the form of Eq. 2.9, with 3 different Ω_B^i, ω_1^i and ω_2^i with i = axial, radial 1, radial 2. Therefore, for a given set of voltages, we can calculate the Hessian of the field along with the Coulomb interaction, extract the frequencies and coupling rates from the eigenvalues of the 3x3 submatrices for each directional mode, and use $\frac{\Delta\omega^i}{\Omega_B^i}$ for one specific mode i as a cost measure.

However, the previous method is susceptible to small deviations of the approximation. If the applied voltages would produce a slightly twisted potential, then using a cost function that relies on the approximation of having the ions displaced in the same direction will produce significantly changed coupling rates. Another method that is not based on this approximation is based on the participation rates discussed in Chapter 2. In fact, experimental measurability makes this metric particularly appropriate for our purposes. To determine the participation rates, one need only diagonalize the 3Nx3N total hessian, group the resulting modes into pairs of out-of-phase and in-phase modes, and compare the norm of the block vectors corresponding to the motion of each ion for each pair. In practice, we will use this method and maximize the participation rates. Furthermore, later on, to limit motional decoherence, heating and dephasing we ideally do not want to move the ions while switching the beamsplitter, thus, to ensure that the optimizer is not decoupling the ions by separating them spatially, we also add a cost term that tries to minimize the interion distance.

3.1.2 Results

One of the found voltage settings using the participation rates approach is depicted in Figure 3.2. For this setting the equilibrium distance is 16.96 µm with a maximal participation rate of 94.62% for the radial mode with mean frequency 2.33 MHz.

We used an empirically determined weighting of each cost term, a starting point where all voltages were at 4V except the middle electrode that was at 0V to have a confining starting potential. The optimization was done using the scipy.optimize "Nelder-Mead" method, which is a local optimizer. More information about the code can be found at [22]. We also observe that the optimizer found a solution that locally looks like a third order potential to allow for maximal potential offset difference between both ions, this hints that we can describe our search space in a more sophisticated way. We will discuss this in the next section.

[2]The hessian of the potential of the electrodes summed with the hessian of the coulomb interaction of the ions.

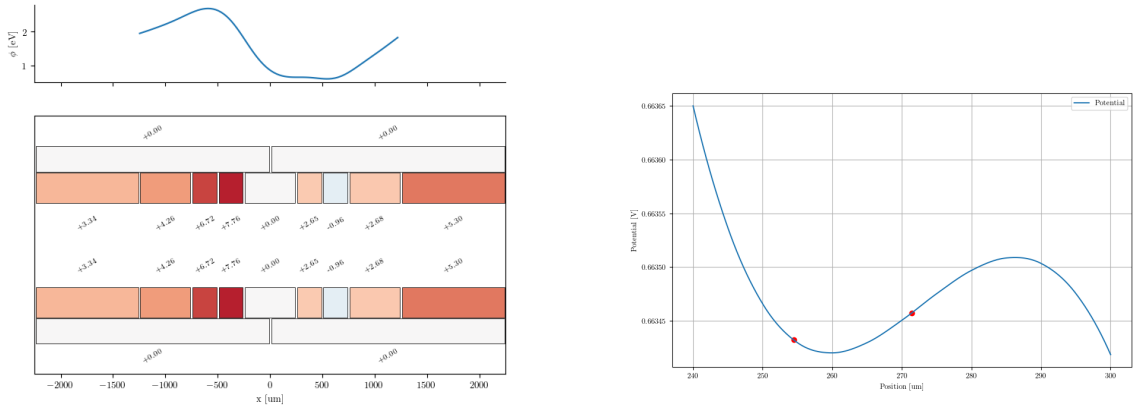

a) b)

Figure 3.2: Illustration of the optimized voltage settings in the trap for maximal participation rate and the resulting ion positions. Subplot a) showcases the voltage settings, which yield an equilibrium distance of 16.96 µm and a maximal participation rate of 94.62% for the radial mode with a mean frequency of 2.33 MHz. Subplot b) provides a zoomed-in view of the potential, indicating the positions of the ions as two red points.

3.2 Optimization over orders of the applied potential

As already hinted at by the results of the naive optimization of the previous section, it seems that for the allowed voltage range and our electrode size, the changes of the potential on distances of orders of tens of µm can be approximated by a polynomial of up to fourth order. This will not only simplify the numerical optimization and allow for a better theoretical understanding but also make the experimental implementation more adaptable. Consequently, instead of optimizing over a search space of dimension 9 we can reduce it to a search space of dimension 5.

3.2.1 Abstract potentials

To model the system up to the fourth order, we created a class of abstract 3D potentials, where each produces one of the orders of a polynomial

$$V(x) = a_0 + a_1 x + a_2 x^2 + a_3 x^3 + a_4 x^4. \tag{3.1}$$

in the axial plane for $y, z = 0$. The rest of the potential that goes in the radial directions has either been fully fixed by the Laplace equation

$$\nabla V(x, y, z) = 0 \tag{3.2}$$

or chosen such that the resulting potential is symmetric. Thus, instead of summing the potentials of each electrode with some weights, we now parametrize our potential with weights for each order and then using the same cost function as before optimize for the best prefactors. Once we have the theoretical best abstract potential, we fit it with the PyTrans [23] software, which is using the already simulated potentials of each electrode and then optimizes each voltage to reach the

predefined potential.

3.2.2 Results

In practice, we firstly saw that the abstract optimization mostly tended to find a double well potential, which consists of a positive quartic and a negative quadratic, where one well had an offset compared to the other. However, the resulting PyTrans fit of such a quartic potential was very faulty, which is mainly due to the difficulty of fitting a fourth order up to a certain strength with limited voltages. Accordingly, we focused on the optimization of abstract potentials containing only up to a cubic term. One of the found abstract potentials can be seen in Figure 3.3, it has the following prefactors:

axial offset [MHz]	axial field [$\mathrm{V\,m^{-1}}$]	axial frequency [MHz]	axial cubic [10^{12} $\mathrm{V/m^3}$]
0.28246685	-4.63952246	0.66582342	0.66663661.

The resulting equilibrium distance is 20.06 µm with a maximal participation rate of 93.02% for the radial mode with mean frequency 2.28 MHz.

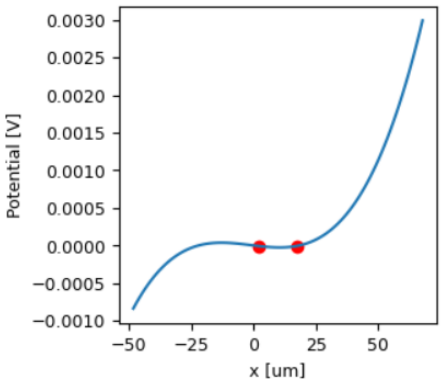

Figure 3.3: Plot of the optimized abstract potential in the axial plane, which yields an equilibrium distance of 20.06 µm with a maximal participation rate of 93.02% for the radial mode with mean frequency 2.28 MHz. The positions of the ions are indicated as two red points.

The PyTrans fit that we get with our electrodes can be seen in 3.4. The potential looks pretty similar at first sight, however the numerical analysis give us an equilibrium distance of 11.25 µm and a max. participation rate of 71.01%. This different result comes from the difficulty to fit an arbitrary abstract potential with our finite numbered and sized electrodes. This difficulty will be further emphasized in the next section.

An interesting approach that one could consider is to first find an optimized abstract potential, fit it using PyTrans, and then implement a feedback loop in the experiment to run an optimization over the voltages to "polish" the fit. If one already has a good initial guess, a local optimizer like "Nelder-Mead" is sufficiently powerful and could potentially be fast enough to allow for a quite reasonable fine-tuning. Tests of this approach can be found on the project repository [22].

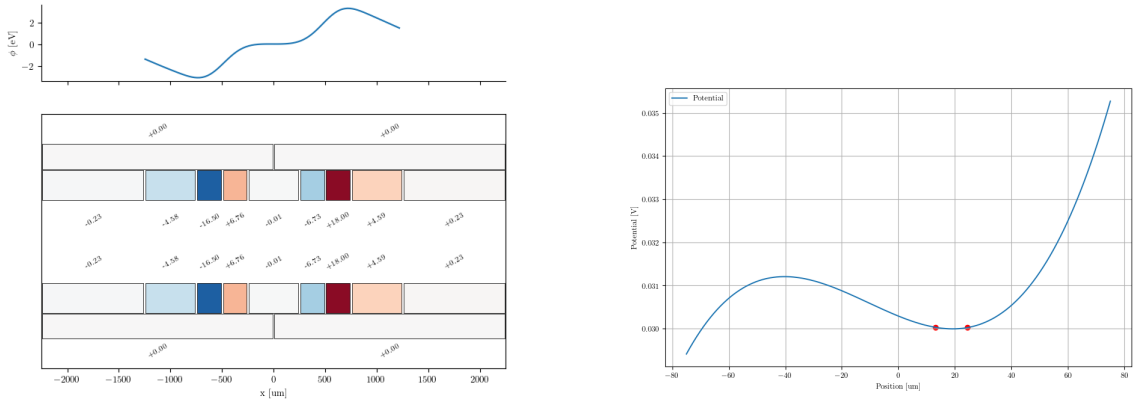

a) b)

Figure 3.4: Illustration of the resulting PyTrans potential fit of the optimized abstract potential of Figure 3.3. Subplot a) showcases the voltage settings, which yield an equilibrium distance of 11.25 µm and a maximal participation rate of 71.01%. Subplot b) provides a zoomed-in view of the potential, indicating the positions of the ions as two red points.

3.3 Limitations of numerical simulations

In this section, we will discuss aspects that limit the applicability of the proposed numerical approaches.

Regarding the first approach of naively optimizing the voltages without molding the search problem to a physical interpretation, we noted that slight variations of 0.1 volts in the applied voltages could lead to quite significant participations rate changes of up to 30%. This is rather undesirable for the experimental setup, as we will not exactly have the given voltages and thus the experimental coupling could be quite different from the numerical approximation. Additionally, as we do not have a direct understanding of the action on the ion of each voltage, it is hard to counteract experimental variations. To address that issue, it would be firstly interesting to do a noise analysis of the solutions by introducing slight variation in the voltages and seeing how the solutions are affected and eventually to search for solutions that are more noise-resilient. Another approach that could be taken is similar to the proposed "polishing", it would consist of an experimental feedback loop to optimize over the voltages in the experiment to compensate for voltage variations.

A big limiting factor for the abstract potential approach is given by our ability to fit a generic potential given our trap capabilities. In fact, a big factor that influences the quality of the fit is where in the trap we locally fit. This comes naturally considering that the electrode sizes are not identical, thus depending on the parity of the to-be-fitted potential different trap positions are beneficial. In Figure 3.5 one can find the optimal strength bounds and positions in the trap dependent on what potential terms need to fitted. One can see that, for a high quartic and a high cubic, fitting around 325 µm seems to be much more adapted for quartic potentials than the position of 593 µm that is currently being used in the experiments.

Lastly, one big limiting factor that remains is related to the trap model that we are using. The

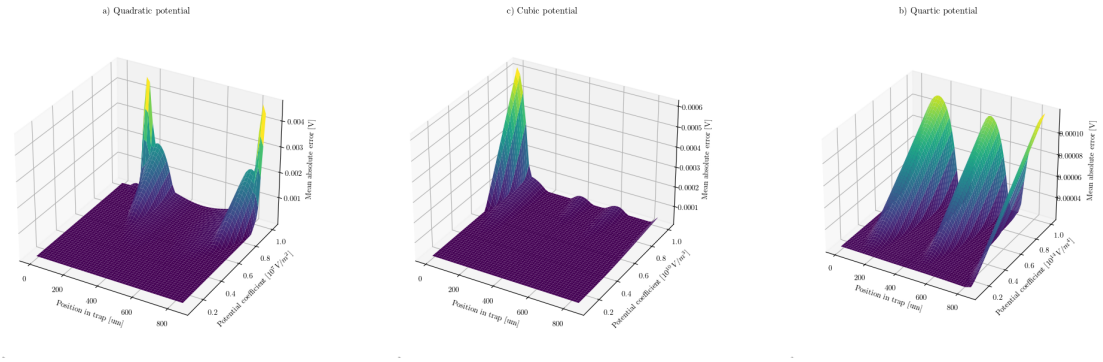

Figure 3.5: 3D visualization of Mean Absolute Fit Errors for different potential orders. The subplots from a) to c) represent the quadratic, quartic, and cubic potentials respectively. The X-axis represents the position in the trap in micrometers, the Y-axis displays the potential coefficient in varying units, and the Z-axis depicts the Mean Absolute Error in Volts. The color map 'viridis' is used to visually distinguish the error magnitude. As can be seen from the three subplots, the influence of potential order on mean absolute error varies significantly, providing a comprehensive overview of the fitting performance under different conditions."

potential for each electrode has been modeled on a grid of approximate axial resolution of 30 µm, this could already cause troubles if we are trying to get equilibrium positions of around 20 µm. Furthermore, it would be reasonably beneficial to experimentally verify the model. To do so, one could think of probing some positions in the axial direction with one ion in a quadratic well, and then at each position slightly modify each electrode and measure the radial frequency splitting to quantify the offset, displacements to quantify stray fields and the axial frequency to quantify stray quadratures. Then one could feed the data back in the model and tune it correspondingly.

Chapter 4

Experimental decoupling results

This chapter highlights our experimental attempts to achieve an uncoupled system. Due to limitations from numerical simulations, as noted in Section 3.2, we focus on strategies involving voltage control through potential orders. Hence, the applied potential is parametrized as a fourth-order polynomial in the axial plane, as shown:

$$V(x) = a_0 + a_1 x + a_2 x^2 + a_3 x^3 + a_4 x^4. \tag{4.1}$$

Here, a_0, a_1, a_2, a_3 and a_4 represent the individually tunable coefficients for each term in the potential, allowing us to carefully tailor the potential in our experiments. Each order has then been fitted axially with PyTrans and the tunable coefficients have been implemented in our experiment interface.

Three aspects are discussed, namely, firstly trapping two ions at an equilibrium positions of approximately 12 µm and detuning the radial of the two ions by gradually adding a third order. With this approach, we reach a decoupling factor $\Delta\omega/2\Omega_B$ of 2.05 which would result in a theoretical by 50% reduced energy exchange. Secondly, we also discuss our attempts to handle a double well setup and address limitations. Finally, we will present results of two ions in a setting similar to the first part, but with a shallower quadratic to have higher ion distances. We argue why this would in theory allow for higher decoupling. However, we also present experimental results where we only reach a decoupling factor $\Delta\omega/2\Omega_B$ of 1.55 and discuss the mismatch to the numerical simulations.

4.1 Third order potential decoupling

As seen in the numerical analysis, it seems best to start with just a quadratic potential and get the asymmetry for our detuning for an added third order. This also seems to be beneficial as our electrodes are struggling to simulate a fourth order potential on the length scales we need. Consequently, we firstly loaded two ions in the trap in a 0.3 MHz quadratic potential, then we scanned the cubic prefactor stepwise around 0 up to $\pm 0.4 \cdot 10^{11} \mathrm{V/m^3}$, and measured positions of the ions and mode frequencies at each step. This is approximately the maximal range for the cubic term for that quadratic strength, as increasing it further would result in a non-confining potential.

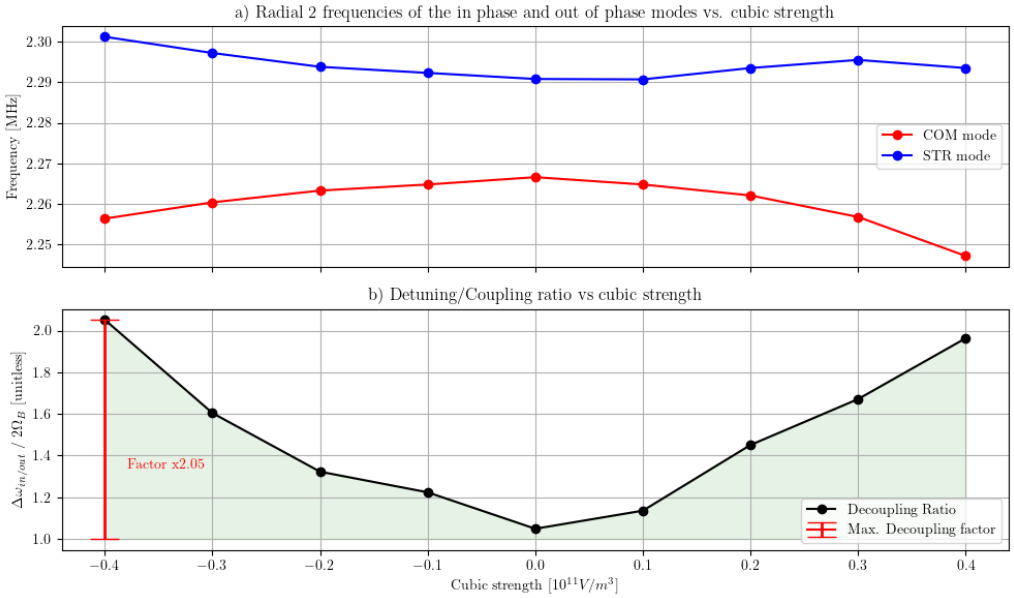

Figure 4.1: Coupling analysis for two ions with equilibrium distance (11.90 ± 0.11) µm in a 0.3 MHz quadratic potential with changing cubic potential of strength up to $\pm 0.4 \cdot 10^{11}\mathrm{V/m^3}$. (a) Mode frequencies of in-phase and out-of-phase modes of the second radial mode, demonstrating an anti-crossing diagram, with the waist representing a coupling of 24.2 kHz. (b) Detuning divided by $2\Omega_B(s_0)$, illustrating a maximal decoupling factor $\Delta\omega/2\Omega_B$ of 2.05 resulting in theoretical oscillations with a reduced contrast of 0.49.

To measure the positions, we proceeded as explained in Chapter 2, and the mode frequencies were measured by scanning an offset carrier frequency to resolve the RSB. We adjusted first and second order terms to keep the interion distance constant at (11.90 ± 0.11) µm. This was done initially to be able to plot an anti-crossing diagram where a constant coupling strength is needed. However, to factor out fluctuating distances, we later on opted to plot the detuning, which can be calculated from the interion distance and the radial modes' frequencies.

The mode frequencies of the in phase and the out of phase modes of the second radial mode with mean frequency 2.28 MHz can be seen in Figure 4.1 a). As the distance is approximately constant for each cubic term, this can be regarded as an anti-crossing diagram, where the waist corresponds to a coupling of $2\frac{\Omega_B}{2\pi} = 24.2\,\mathrm{kHz}$. For the corresponding distance of 11.84 µm we would expect a coupling of $2\frac{\Omega_B^{id}}{2\pi} = 23.1\,\mathrm{kHz}$, thus the results correspond to the theory.

In figure 4.1 b) the detuning divided by $2\Omega_B(s_0)$ is depicted. We can see that the maximal decoupling factor $\Delta\omega/2\Omega_B$ is 2.05, however, this factor is not enough to reach the uncoupled setting $\Delta\omega >> \Omega_B$. In fact, if comparing with Eq. 2.14, we can see that one excitation in mode 1 would be transferred with a factor of $\frac{1}{2.05} = 0.49$ to mode 2 after a time of $\tau = \frac{\pi}{2 \cdot 2.05 \cdot \Omega_B} \approx 10\,\mu\mathrm{s}$.

4.2 Double well potential

As seen in the above section, the resulting decoupling factor $\Delta\omega/2\Omega_B$ of only using a quadratic and then adding the asymmetry in the system through a cubic potential is not big enough in our setup to allow for a good enough decoupled setting. But as the decoupled setting is dependent on the detuning of the frequencies and the coupling strength, it seems reasonable to consider working in a regime where the coupling is lower. This is achieved by increasing the equilibrium distance of our ions. However, as our final goal is a switchable interaction for a two-qubit gate where we ideally do not move the ions, we should work with a distance that gives a strong enough coupling strength such that the gate does not take too long. Consequently, we ideally do not want to exceed distances of 20 µm to have a coupling rate above 2 kHz.

One way to achieve a setting where the equilibrium distances are increased compared to the quadratic plus cubic potential is a double well configuration. That this configuration is useful for a detuning was already hinted at by our numerical simulations of abstract potentials. In theory, one could create a detuning by adding a linear term or a cubic term to the double well, where in both cases the double well will be tilted and one well will be at a higher potential than the other, resulting in the wanted detuning of the radial modes. However, in practice, working with a double well with our setup has proven to bring big challenges with it.

The first problem that appeared was that, at the trap position of 593 µm we were not able to generate a double well that had an equilibrium distance below 35 µm. This approximate minimal distance corresponded to numerical simulations and was mainly due to the fact that we could not generate enough quartic strength to bring the coulomb repulsed ions closer together. However, this distance would still be conceivable for our purposes, and thus we still went on. However, the next limitation came from the micromotion compensation and the cooling, which we did not manage to correctly get working. We suspect that this is due to the low axial frequency the ions are experiencing if the inverse quadratic is set too low to reduce the ion distance. Consequently, we took the decision to use the numerical simulations and find a trap zone where we could increase the quartic strength. Nevertheless, we only managed to find a region at 325 µm where the quartic strength could be increased by a factor of 2. And even if this factor seems enough at first glance, it would only allow for a reduction of the distance of a factor $1/\sqrt{2} \approx 0.7$, thus, theoretically allowing for distances of 25 µm. Furthermore, the curvatures at the double well minima are given by $4a_2$, but since the frequency is proportional to the square root of the curvature, we would likewise only increase the axial frequency by a factor of $1/\sqrt{2} \approx 0.7$. Hence, instead of pursuing the double well, where we would only be able to have distances of 25 µm and above and be in an unknown potential type where we are not exactly sure how to cool and compensate the micromotion correctly we decided instead to return to the quadratic and increase the ion distance by reducing the quadratic strength.

4.3 Increased distance third order decoupling

Another attempt we thought of was to work with lower quadratic potentials, this would, in theory, allow us to repeat the experiment of Section 4.1 but with a bigger distance. However, it would

also mean that we can apply less third order before the trap become too shallow as the depth of the potential scales like ω_x^4/a_3.

To better understand the dependence of the possible decoupling on the quadratic strength we are working with, we numerically found for a list of quadratic frequencies each corresponding maximal third order potential that we can apply before two ions are not confined anymore. Then, with that maximal third order strength, we computed the resulting potential difference at the ion equilibrium positions. This potential difference should be linear in the detuning of the radial modes, according to 3.1. Finally, by multiplying this potential difference by the distance cubed, we get a quantity that is proportional to the decoupling factor $\Delta\omega/2\Omega_B$. Results of these numerical calculations are shown in 4.2. In subplot a) we can see that the voltage difference is increasing with higher quadratic frequencies. This is to be expected as with higher quadratic the max third order is higher and, thus, the possible voltage difference is increasing as well. In fact, we see that the exact relation between the voltage difference and the axial frequency is $\Delta V \propto \omega_x^{2/3}$. In subplot b) we see that the equilibrium distance goes as $s_0 \propto \omega_x^{-2/3}$ in accordance with the theory of a pure quadratic potential [11]. Finally, we plot $\Delta V \cdot s_0^3 \propto \Delta\omega/2\Omega_B$ in subplot c). There we see that the decoupling factor $\Delta\omega/2\Omega_B$ is proportional to $\omega_x^{-4/3}$, thus in theory we see that it is advantageous to work in regimes with lower quadratic potentials.

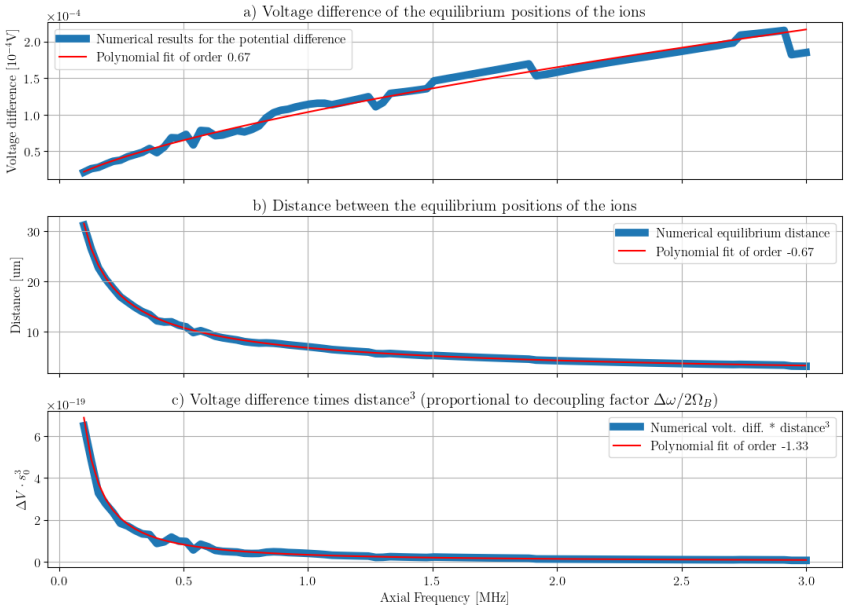

Figure 4.2: Numerical calculations illustrating the relationship between quadratic frequencies, the potential difference at ion equilibrium positions, and decoupling. Subplot a) demonstrates the increase in voltage difference with higher quadratic frequencies, showing a relationship of $\Delta V \propto \omega_x^{2/3}$. Subplot b) displays the equilibrium distance relation $s_0 \propto \omega_x^{-2/3}$, consistent with the theory for a pure quadratic potential. Subplot c) shows $\Delta V \cdot s_0^3$, proportional to the decoupling factor $\Delta\omega/2\Omega_B$, revealing a dependence on $\omega_x^{-4/3}$. These findings suggest an advantage in working within regimes with lower quadratic potentials.

To verify if we would have better decoupling rates for lower axial potentials, we started by loading

two ions in a 0.2MHz quadratic potential, and then we scanned the cubic factor as high as experimentally possible. Numerically, we expect the maximal cubic strength to be around $9.03 \cdot 10^9 \mathrm{V/m}^3$, however, experimentally we did not manage to get much more than half that strength, namely around $5 \cdot 10^9 \mathrm{V/m}^3$. Even if the maximal cubic strength is a bound as we might lose the ions earlier due to heating, scattering of photons, etc., we suspect that the voltages for our third and second orders are not exactly corresponding to the theory and thus, especially for low strengths, we get undesired effects that affect the stability. This is also indicated by the increasing equilibrium distance with increasing third order that we see in the experiments and which should not be happening. Nevertheless, we still tried to repeat the results from Section 4.1. To do so, we gradually increased the third order strength and measured positions and mode frequencies[1] of both radials with both ions[2] at each step.

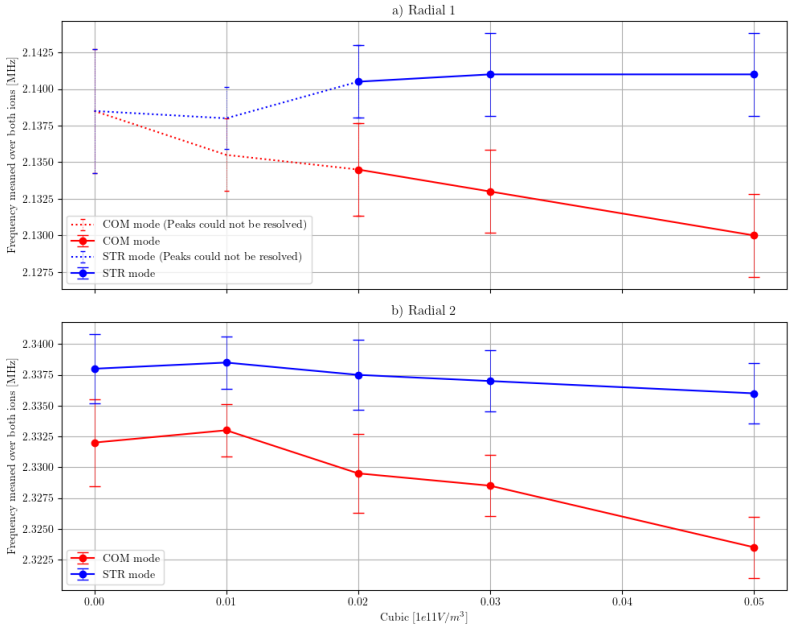

Figure 4.3: Mode frequencies of in-phase and out-of-phase modes of both radials in a 0.2 MHz quadratic potential with changing cubic strength. The modes could not be resolved for the first 2 data points of radial 1. For radial 2 the waist corresponds to a coupling rate of $2\frac{\Omega_B}{2\pi} = (6 \pm 5)$ kHz, which is consistent with the expected coupling of $2\frac{\Omega_B^{id}}{2\pi} = 7.27$ kHz for the corresponding distance of 17.4 µm.

A plot of the in phase and out of phase mode frequencies for both radials can be seen in Figure 4.3. Nevertheless, in contrast to the previous experiment, we did not correct the quadratic strength to keep a constant distance, thus, the plot cannot be directly interpreted as an avoided crossing diagram as the coupling rate is not constant. Furthermore, for radial 1 the separation of the in phase and out of phase mode frequency peaks was not possible for the first 2 data points for at least 1 ion. This was probably due to our short RSB pulses. However, for radial 2 the peaks could be resolved for 0 cubic strength, resulting in a mode splitting of $2\frac{\Omega_B}{2\pi} = (6 \pm 5)$ kHz. For the

[1] We asserted the error of the frequency of taking the FWHM of each peak. The big uncertainty comes from the small separation in frequency of the two peaks.

[2] We later on took the mean of the two frequencies that we got from the two different ions.

corresponding distance of 17.4 µm, we expect a coupling rate of $2\frac{\Omega_B^{id}}{2\pi} = 7.27\,\text{kHz}$, thus the results are coherent with the theory.

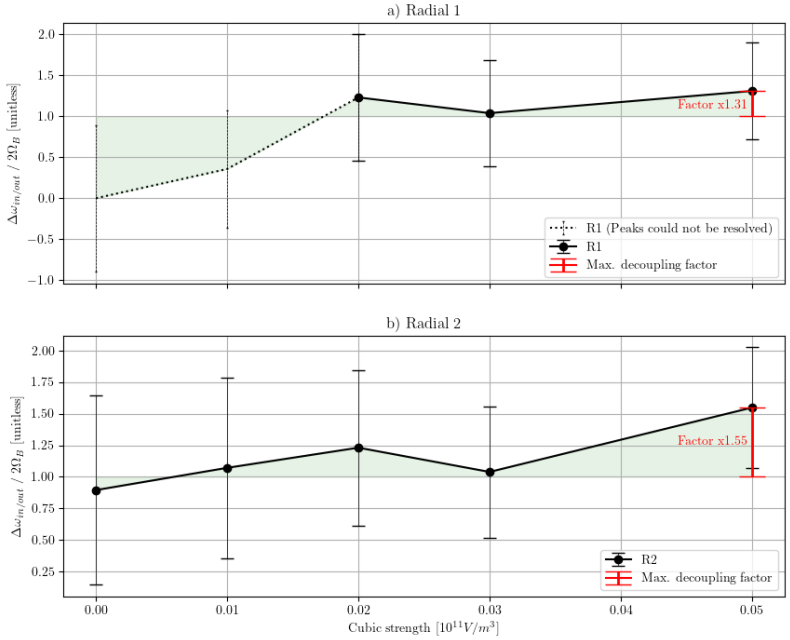

Figure 4.4: Evaluation of the decoupling factor $\Delta\omega/2\Omega_B$ under varying cubic strength for two different radials at a 0.2 MHz quadratic potential. The analysis illustrates the maximal decoupling factor $\Delta\omega/2\Omega_B$ achieved, corresponding to a theoretical energy exchange of 0.65. Despite numerical expectations, the results indicate a higher contrast, likely influenced by the lower stable cubic strengths attained during the experiments.

The decoupling factor $\Delta\omega/2\Omega_B(s_0)$ as a function of the cubic strength is depicted in Figure 4.4. Here we see that the maximal decoupling factor $\Delta\omega/2\Omega_B$ that we reach with a quadratic potential of 0.2 MHz is 1.31 for the radial of mean frequency 2.33 MHz and 1.55 for the radial of mean frequency 2.11 MHz. This would correspond to a reduced contrast of $\frac{1}{1.55} = 0.65$. Contrary to our numerical expectations as seen in 4.2, this would result in a higher theoretical energy exchange contrast than for our experiment at 0.3 MHz, however, as discussed before this is probably due to the low stable cubic strength that we did not manage to surpass in the experiments.

Chapter 5

Conclusion and Outlook

During this project, we tried different approaches to reach a tunable beamsplitter interaction to be used later on in a two-qubit gate between GKP encoded qubits. At first, we presented an analytical analysis detailing the ways in which Coulomb interaction induces a beamsplitter interaction, along with the parameters that influence ion coupling. Furthermore, we highlighted two analytical metrics to quantify the level of coupling and discussed how to validate them experimentally. Secondly, we showed numerical methods and optimization results where we reached theoretical modal participation rates of below 6% for interion distances of 17 µm for the uncoupled setting. We also proposed various numerical analyses, including examining the mode splitting response to voltage offset increases. This revealed a linear relationship between the change in radial mode frequency and voltage offset. We also evaluated the fitting performance of different potential types on the electrodes. Through this, we identified trap zones capable of achieving order-potentials larger by a factor two. Finally, we analyzed the quadratic strength-dependent maximally reachable decoupling. This showed that in a system governed by both a quadratic and third-order potential, better decoupling can be theoretically achieved at lower quadratic strengths. Finally, we presented experimental results demonstrating noticeable $\Delta\omega/2\Omega_B$ factors. Specifically, we achieved a factor of up to 2.05, leading to an energy exchange reduction of more than 50% for a 0.3 MHz quadratic potential. Further, we obtained a decoupling factor of up to 1.55, which resulted in a 35% reduction in energy exchange for a 0.2 MHz quadratic potential. We also discussed the challenges and limitations encountered in our attempts to reach an uncoupled regime using a double well potential.

The detuning we reached in the experiment are insufficient for a switchable beamsplitter interaction. Several strategies could potentially help attain a better level of decoupling. For instance, working with even lower quadratic potentials could be considered, ensuring that the fitting of the quadratic and cubic potential is optimized for such lower strengths. Alternatively, employing higher distance double wells with the addition of a third order could be explored, as this setup seems to naturally facilitate detuning. Finally, an experiment where the interion distance is changed in-sequence could be envisaged to manipulate the distance, hence controlling the coupling rate.

Bibliography

[1] V. V. Albert, K. Noh, K. Duivenvoorden, D. J. Young, R. T. Brierley, P. Reinhold, C. Vuillot, L. Li, C. Shen, S. M. Girvin, B. M. Terhal, and L. Jiang. Performance and structure of single-mode bosonic codes. *Physical Review A*, 97(3), mar 2018.

[2] R. A. Berner. Gkp-setup imaging system and single ion addressing with an aod. Research internship report, TIQI Group, ETH Zürich, July 2022.

[3] K. R. Brown, C. Ospelkaus, Y. Colombe, A. C. Wilson, D. Leibfried, and D. J. Wineland. Coupled quantized mechanical oscillators. *Nature*, 471(7337):196–199, Mar. 2011.

[4] B. de Neeve, T. L. Nguyen, T. Behrle, and J. Home. Error correction of a logical grid state qubit by dissipative pumping, 2020.

[5] D. P. DiVincenzo. The physical implementation of quantum computation. *Fortschritte der Physik*, 48(9-11):771–783, sep 2000.

[6] C. Flühmann. *Encoding a qubit in the motion of a trapped ion using superpositions of displaced squeezed states.* Doctoral thesis, ETH Zurich, Zurich, 2019.

[7] C. Flühmann, T. L. Nguyen, M. Marinelli, V. Negnevitsky, K. Mehta, and J. P. Home. Encoding a qubit in a trapped-ion mechanical oscillator. *Nature*, 566(7745):513–517, feb 2019.

[8] D. Gottesman, A. Kitaev, and J. Preskill. Encoding a qubit in an oscillator. *Physical Review A*, 64(1), jun 2001.

[9] D. Kienzler. Trapped-ion physics lecture, February 2023. Lecture Notes for Trapped Ion Physics Lecture.

[10] R. Lechner, C. Maier, C. Hempel, P. Jurcevic, B. P. Lanyon, T. Monz, M. Brownnutt, R. Blatt, and C. F. Roos. Electromagnetically-induced-transparency ground-state cooling of long ion strings. *Phys. Rev. A*, 93:053401, May 2016.

[11] T. P. Meyrath and D. F. James. Theoretical and numerical studies of the positions of cold trapped ions. *Physics Letters A*, 240(1):37–42, 1998.

[12] M. A. Nielsen and I. L. Chuang. *Quantum computation and quantum information.* Cambridge University Press, Cambridge ; New York, 10th anniversary ed edition, 2010.

[13] K. Noh, V. V. Albert, and L. Jiang. Quantum capacity bounds of gaussian thermal loss channels and achievable rates with gottesman-kitaev-preskill codes. *IEEE Transactions on Information Theory*, 65(4):2563–2582, apr 2019.

[14] J. Preskill. Quantum computing 40 years later, 2023.

[15] S. Ragg, C. Decaroli, T. Lutz, and J. P. Home. Segmented ion-trap fabrication using high precision stacked wafers. *Review of Scientific Instruments*, 90(10):103203, 10 2019.

[16] M. Reiher, N. Wiebe, K. M. Svore, D. Wecker, and M. Troyer. Elucidating reaction mechanisms on quantum computers. *Proceedings of the National Academy of Sciences*, 114(29):7555–7560, jul 2017.

[17] S. R.-K. Rodriguez. Classical and quantum distinctions between weak and strong coupling. *European Journal of Physics*, 37(2):025802, jan 2016.

[18] I. Rojkov, P. M. Röggla, M. Wagener, M. Fontboté-Schmidt, S. Welte, J. Home, and F. Reiter. Two-qubit operations for finite-energy gottesman-kitaev-preskill encodings, 2023.

[19] P. W. Shor. Polynomial-time algorithms for prime factorization and discrete logarithms on a quantum computer. *SIAM Journal on Computing*, 26(5):1484–1509, 1997.

[20] V. V. Sivak, A. Eickbusch, B. Royer, S. Singh, I. Tsioutsios, S. Ganjam, A. Miano, B. L. Brock, A. Z. Ding, L. Frunzio, S. M. Girvin, R. J. Schoelkopf, and M. H. Devoret. Real-time quantum error correction beyond break-even. *Nature*, 616(7955):50–55, mar 2023.

[21] H. Timme. Single-ion addressing using crossed acousto-optic deflectors. Master's thesis, ETH Zürich, Department of Physics, Trapped Ion Quantum Information Group, March 2023.

[22] TIQI Projects. GKP Trap Model. `https://gitlab.phys.ethz.ch/tiqi-projects/gkp/lab/gkp-trap-model.git`, 2023. Accessed: August 17, 2023.

[23] TIQI Projects. Pytrans2. `https://gitlab.phys.ethz.ch/tiqi-projects/pytrans2.git`, 2023. Accessed: August 17, 2023.

[24] K. Toyoda, R. Hiji, A. Noguchi, and S. Urabe. HongâOuâMandel interference of two phonons in trapped ions. *Nature*, 527(7576):74–77, Nov. 2015.

Eidgenössische Technische Hochschule Zürich
Swiss Federal Institute of Technology Zurich

Title of work:

Towards a tunable beamsplitter interaction between two radial modes of two ions for GKP qubits

Thesis type and date:

Semester Thesis, July, 2023

Supervision:

Martin Wagener, Moritz Fontboté-Schmidt, Dr. Stephan Welte
Prof. Dr. Jonathan Home

Student:

Name: Maurice D. Hanisch
E-mail: mhanisc@student.ethz.ch
Legi-Nr.: 22-956-379

Statement regarding plagiarism:

By signing this statement, I affirm that I have read and signed the Declaration of Originality, independently produced this paper, and adhered to the general practice of source citation in this subject-area.

Declaration of Originality:

`http://www.ethz.ch/faculty/exams/plagiarism/confirmation_en.pdf`

Zürich, 17. 8. 2023: